Supplementary materials to: High-frequency variability dominates potential connectivity between remote coral reefs

Noam Vogt-Vincent[1], Satoshi Mitarai[2], and Helen Johnson[1]

[1]Department of Earth Sciences, South Parks Road, University of Oxford, Oxford, UK
[2]Marine Biophysics Unit, Okinawa Institute of Science and Technology Graduate University, Tancha, Okinawa, Japan

Text S1: Larval dispersal component of SECoW

The larval dispersal component of SECoW assumes that coral larvae physically behave as positively buoyant, otherwise passive particles, which are advected by surface currents for 120 days after spawning, using a fourth-order explicit Runge-Kutta scheme in OceanParcels. Coral larvae are weak swimmers compared to horizontal ocean currents (Kingsford et al., 2002; Hata et al., 2017) but the vertical position of coral larvae in the water column is more challenging to constrain. Although newly fertilised coral eggs are generally positively buoyant (Szmant and Meadows, 2006), larvae tend to lose buoyancy as they develop (Harii and Kayanne, 2003; Szmant and Meadows, 2006). However, the swimming speed of coral larvae can be significant compared to vertical velocities in the ocean (Hata et al., 2017), facilitating some measure of control over their vertical position in the water column. Under controlled conditions, some coral larvae move downwards towards settlement tiles after days to weeks (Szmant and Meadows, 2006; Tay et al., 2011) whereas others have been observed to actively swim upwards towards the light, with no dependency on larval age (Mulla et al., 2021). Regardless, little is known about the vertical positioning of coral larvae in the open ocean so, for practical reasons (the excessive storage requirements of storing high-frequency 3D velocity fields for such a high-resolution domain, and the experimental flexibility offered by an offline particle tracking approach), in this study we assumed that they remain near the ocean surface. We did not use a parameterisation for sub-grid scale processes, as it is not clear that a simple random walk parameterisation would result in any meaningful improvement at the relatively high resolution and short connectivity timescales used in this study (Okubo, 1971; van Sebille et al., 2018; Reijnders et al., 2022). Using a stochastic parameterisation would also require an additional (and arbitrary) parameterisation to prevent particles from entering land cells, and any uncertainty introduced by not resolving sub-grid scale processes is likely small compared to the biological uncertainties described above.

We released particles from every c. 2×2 km reef cell on the WINDS grid, based on an upscaled reef cover map derived from satellite imagery (Li et al., 2020). The resulting reef cover is likely higher than the actual coral cover (and clearly higher than the coral cover for any one species), but we choose this approach to broaden the applicability of our results, as taking subsets from the full dataset is straightforward. The Li et al. (2020) reef map is provided at a significantly higher resolution than WINDS, so some reefs are identified by the WINDS land-sea mask as being on land. In these cases, we redistributed the 'land' reef area onto the nearest ocean cells to conserve the total reef area (in rare cases, this results in an apparent reef

cover >100%), resulting in 8088 reef cells across the WINDS domain. We released $N = 1024$ (32×32) particles per reef cell, arranged in a regular grid, and simulated daily spawning events at midnight from 1 January 1993 to 31 December 2019, for a total of 9861 domain-wide spawning events, with c. 8.3×10^6 particles seeded per event.

Each particle represents a large number of coral larvae, assumed to have an initial separation small enough such that they do not disperse significantly relative to one another. In the present study, we assumed a constant coral fecundity per unit area per day, ρ. The computation of larval fluxes between cells necessitates a value for ρ, which we set to $\rho = 1$ larva m^{-2} d^{-1}, but this value does not affect any patterns or trends in this study as long as it is constant. In reality, coral fecundity is certainly not constant (e.g. Hartmann et al., 2018), but this is a necessary approximation for now, as no maps of coral fecundity exist spanning the southwest Indian Ocean. Therefore, each particle released in cell i represents $L_i^0 = \rho A_i/N$ larvae at spawning, where A_i is the reef cover of cell i for the purpose of this study.

Following Connolly and Baird (2010), we assumed that the coral larvae represented by each particle are split across three larval reservoirs: a pre-competent reservoir L_1, a competent reservoir L_2, and a post-competent or dead larval reservoir L_3. The pre-competent and competent reservoirs evolve through time according to the following differential equations:

$$\frac{dL_1}{dt'} = -\alpha^*(t')L_1(t') - \mu_m(t')L_1(t') \tag{1}$$

$$\frac{dL_2}{dt'} = \alpha^*(t')L_1(t') - \beta L_2(t') - \mu_m(t')L_2(t') - \mu_s F_r(t')L_2(t') \tag{2}$$

$$\alpha^*(t') = \begin{cases} 0 & t' < t_c \\ \alpha & t' \geq t_c \end{cases}$$

Where α^* is a competency acquisition rate (d^{-1}), β is a competency loss rate (d^{-1}), μ_m is a mortality rate (d^{-1}), μ_s is a settling rate (d^{-1}), and F_r is the fraction of a WINDS cell area covered by reef. The parameter a^* is equal to 0 before a larva has reached its minimum competency period t_c (d), and α thereafter. The settling term $\mu_s F_r(t) L_i^2(t)$ was not present in the original formulation of Connolly and Baird (2010). Since SECoW cannot provide any physical insight into the position of a particle below the WINDS grid resolution (c. 2km), we assumed that the particle is equally likely to be anywhere in the reef cell it currently occupies for the purpose of this biological parameterisation. The settling rate is therefore equal to a fixed settling rate μ_s assuming 100% reef coverage, multiplied by the actual proportion of the reef cell covered by reef. In this study, we set $\mu_s = 1$ d^{-1}, assuming settling times on the order of a day (Tay et al., 2011). However, we also carried out tests with $\mu_s = 0.5$ d^{-1} and $\mu_s = 2$ d^{-1} (see Supplementary Tables 1 – 2), and this primarily affects the absolute number of settling larvae rather than temporal variability. In contrast to assumptions of instantaneous settling (e.g. Holstein et al., 2016; Figueiredo et al., 2022) or use of a Lagrangian Probability Density Function (LPDF, see Mitarai et al. (2009) and applications in Uchiyama et al. (2018); Thompson et al. (2018)), our method accounts for the capacity of upstream reefs to reduce the larval supply to downstream reefs (contrary to the LPDF), whilst sensibly handling sub-grid scale reef coverage and allowing for the possibility of a larva passing over a reef without settling (Hata et al., 2017).

Text S2: Offline computation of coral larval fluxes

We could solve equations 1 and 2 directly by numerically integrating them, either 'online' during particle tracking, or 'offline' after regularly saving particle positions. However, these methods have some significant disadvantages. Integrating these quantities online would require all parameters in equations 1 and 2 to be set before particle tracking. This would limit the applicability of simulation results, since they would have to be rerun for any new sets of parameters. Regularly saving particle positions would require a very high output frequency to integrate equations 1 and 2 without considerable error, which would involve enormous storage requirements. Instead, we can reconstruct the number of larvae settling within a 'settlement event' (defined as a larval particle remaining within a single cell with nonzero F_r^j) by storing only three parameters per event:

- The cell ID (a 16-bit unsigned integer in our configuration, which is used as a key for dictionaries containing the reef area and other parameters)
- The event start time-step (a 16-bit unsigned integer in our configuration)
- The event duration (a 16-bit unsigned integer in our configuration)

Integrating equation 1 with respect to t', letting $L_1(t'=0) = L_0^i$, and defining the survival function $s(t') = e^{-\int_0^{t'} \mu_m(\tau)\ d\tau}$, we obtain

$$L_1(t') = \begin{cases} L_0^i s(t') & t' < t_c \\ L_0^i s(t') e^{-\alpha(t'-t_c)} & t' \geq t_c \end{cases}$$

$L_2(t')$ is only nonzero for $t' > t_c$ and no settlement event can occur for $t' \leq t_c$. We therefore define $t = t' - t_c$ (i.e. the time since the minimum competency period t_c), and set $t \geq 0$. Therefore:

$$L_1(t) = L_0^i s(t+t_c) e^{-\alpha t} \tag{3}$$

Substituting (3) into (2) and solving the resulting differential equation, we obtain the following:

$$L_2(t) = \alpha L_0^i s(t+t_c) e^{-\beta t} e^{-\mu_s \int_0^t F_r(t^*)\ dt^*} \cdot \int_0^t e^{t^*(\beta-\alpha)} e^{\mu_s \int_0^{t^*} F_r(t^{**})\ dt^{**}}\ dt^* \tag{4}$$

We now need to consider the fact that, within a particular settling event $j = 1, 2 \ldots, N$ lasting from τ_0^j to $\tau_0^j + \Delta\tau^j$, $F_r(t) = F_r^j$ is a constant. Therefore, for $\tau_0^j \leq t \leq \tau_0^j + \Delta\tau^j$:

$$\begin{aligned} \int_0^t F_r(t^*)\ dt^* &= \int_0^{\tau_0^j} F_r(t^*)\ dt^* + \int_{\tau_0^j}^t F_r^j\ dt^* \\ &= \phi_0^j + F_r^j (t - \tau_0^j) \end{aligned} \tag{5}$$

where $\phi_0^j = \int_0^{\tau_0^j} F_r(t^*)\ dt^*$ and $\phi_0^{j=1} = 0$. We will now define the outermost integral in (4) as $I_j(t)$, i.e.

$$I_j(t) = \int_0^t e^{t^*(\beta-\alpha)} e^{\mu_s \int_0^{t^*} F_r(t^{**})\ dt^{**}}\ dt^* \tag{6}$$

For $\tau_0^j \leq t \leq \tau_0^j + \Delta\tau^j$, we will split this integral into three sections: $[0,\ \tau_0^{j-1} + \Delta^{j-1}]$ (i.e. up until the end of the last settlement event), $[\tau_0^{j-1} + \Delta^{j-1},\ \tau_0^j]$ (i.e. from the end of the last settlement event to the start of the current settlement event), and $[\tau_0^j,\ t]$:

$$\begin{aligned} I_j(t) = &\int_0^{\tau_0^{j-1}+\Delta^{j-1}} e^{t^*(\beta-\alpha)} e^{\mu_s \int_0^{t^*} F_r(t^{**})\ dt^{**}}\ dt^* \\ &+ \int_{\tau_0^{j-1}+\Delta^{j-1}}^{\tau_0^j} e^{t^*(\beta-\alpha)} e^{\mu_s \int_0^{t^*} F_r(t^{**})\ dt^{**}}\ dt^* \\ &+ \int_{\tau_0^j}^{t} e^{t^*(\beta-\alpha)} e^{\mu_s \int_0^{t^*} F_r(t^{**})\ dt^{**}}\ dt^* \end{aligned} \tag{7}$$

For $\tau_0^j \leq t \leq \tau_0^j + \Delta\tau^j$, we firstly recognise that the first term is equal to $I_{j-1}^{\tau_0^{j-1}+\Delta^{j-1}}$. For the second term, the larval particle is by definition not within a reef cell during the time bounds, i.e. $F_r = 0$, so $\int_0^{t^*} F_r(t^{**})\ dt^* = \phi_0^j$. Therefore, (7) evaluates to:

$$\begin{aligned} I_j(t) &= I_{j-1}^{\tau_0^{j-1}+\Delta^{j-1}} + \int_{\tau_0^{j-1}+\Delta^{j-1}}^{\tau_0^j} e^{t^*(\beta-\alpha)} e^{\mu_s \phi_0^j}\ dt^* + \int_{\tau_0^j}^{t} e^{t^*(\beta-\alpha)} e^{\mu_s (\phi_0^j + F_r^j (t^* - \tau_0^j))}\ dt^* \\ &= I_{j-1}^{\tau_0^{j-1}+\Delta^{j-1}} + \frac{e^{\mu_s \phi_0^j}}{\beta - \alpha} \left[e^{t(\beta-\alpha)} \right]_{\tau_0^{j-1}+\Delta\tau^{j-1}}^{\tau_0^j} + \frac{e^{\mu_s \phi_0^j - \mu_s F_r^j \tau_0^j}}{\beta - \alpha + \mu_s F_r^j} \left[e^{t(\beta-\alpha+\mu_s F_r^j)} \right]_{\tau_0^j}^{t} \end{aligned} \tag{8}$$

Whilst algebraically long-winded, $I_j(t)$ is nevertheless now defined analytically. Therefore, substituting (5) and (6) into (4):

$$L_2(t) = \alpha L_0^i s(t + t_c) e^{-\beta t} e^{-\mu_s \left(\phi_0^j + F_r^j (t - \tau_0^j)\right)} \cdot I_j(t) \tag{9}$$

Finally, from (2) the number of larvae settling during event j, N_s^j, is given by:

$$\frac{dN_s^j}{dt} = \mu_s F_r^j L_2(t) \tag{10}$$

$$N_s^j = \mu_s F_r^j \int_{\tau_0^j}^{\tau_0^j + \Delta\tau^j} L_2(t)\ dt \tag{11}$$

Therefore, to compute N_s^j, we will use the following steps:

1. Retrieve ϕ_0^j and $I_{j-1}^{\tau_0^{j-1}+\Delta\tau^{j-1}}$, both of which were computed in the previous step. Note that both are 0 for $j = 1$.
2. Retrieve F_r^j from the stored cell ID.

3. Integrate (11) numerically.

4. Store $I_j(\tau_0^j + \Delta\tau^j)$ for the next computation.

5. Store $\phi_0^{j+1} = \phi_0^j + F_r^j \Delta\tau^j$ for the next computation.

For reference:

$$N_s^j = c_1 \int_{\tau_0^j}^{\tau_0^j + \Delta\tau_j} f_1(t) \cdot \left(I_{j-1}^{\tau_0^{j-1} + \Delta\tau^{j-1}} + c_2 f_2 + c_3 f_3(t) \right) \, dt$$

$$c_1 = \alpha L_0^i \mu_s F_r^j$$

$$c_2 = \frac{e^{\mu_s \phi_0^j}}{\beta - \alpha}$$

$$c_3 = \frac{e^{\mu_s \phi_0^j - \mu_s F_r^j \tau_0^j}}{\beta - \alpha + \mu_s F_r^j}$$

$$f_1(t) = s(t + t_c) e^{-\beta t} e^{-\mu_s \left(\phi_0^j + F_r^j (t - \tau_0^j) \right)}$$

$$f_2 = \left[e^{t(\beta - \alpha)} \right]_{\tau_0^{j-1} + \Delta\tau^{j-1}}^{\tau_0^j}$$

$$f_3(t) = \left[e^{t(\beta - \alpha + \mu_s F_r^j} \right]_{\tau_0^j}^{t}$$

We compute N_s^j using an explicit fourth-order Runge-Kutta (RK4) scheme. SECoW can use any number of RK4 steps to integrate events, but we found minimal loss of accuracy (compared to direct numerical integration of equations 1-2) by using a single RK4 step (Supplementary Figure 11). In this study, we use five RK4 steps as we had the available computational capacity, but those interested in using SECoW for different biological parameters can use a single step, which generates very similar results. A small number of larger errors can cause unphysical results (e.g. a source strength exceeding 1), but this affects an extremely small number of events (2.4×10^{-5} % for *P daedalea*, 2.0×10^{-5} % for *P daedalea* with a higher settling rate, 2.5×10^{-6} % for *A valida*, and zero for the others). This method of solving for N_s^j is considerably less computationally expensive ($\sim$ 24 hours, parallelised across 27 processes [one per year] on the JASMIN HPC for a single RK4 step per event) than explicitly integrating equations 1 and 2. We store a maximum of 60 events per particle, which captures almost all non-negligible settlement events.

Text S3: Postprocessing of larval fluxes

At source cell i, we release n particles per spawning event. We assume that coral fecundity ρ is directly proportional to reef area, with units larvae m^{-2}. Therefore, the number of larvae initially represented by a single particle generated during a spawning event at source cell i is

$$L_0^i = \rho A_i / n \tag{12}$$

where A_i is the reef area of cell i in m^2, and n is the number of particles released at i (1024). The dispersal script generates a list of settlement events $E_l = (i, j, k, \tilde{N}_l)$, where each settlement event is associated with a source cell i, sink cell j, spawning time k, and generalised larval settlement flux $\tilde{N}_s^l$, where $\tilde{N}_s^l$ is computed from equations 11 and 12, and assuming that $\rho = 1$. In the absence of any better constraints, we assume that $\rho = 1$ for our analyses, and therefore set $N_s^l = \rho \tilde{N}_s^l = \tilde{N}_s^l$.

We will now define the larval flux, F_{ijk}, as the total number of larvae spawning at source cell or group i (at time k) and settling at sink cell or group j:

$$F_{ijk} = \sum^{l} \{N_s^l \mid i, j, k\} \tag{13}$$

Note that since F is computed using a simple summation, i and j in this expression can instead refer to source and sink *groups* (this is not the case for earlier expressions)[1].

Source strength

We define the *raw source strength* of site i, $\underline{S}_{ik}$, as the total number of larvae settling anywhere, given that each larva originated from source cell or group i at time k:

$$\begin{aligned} \underline{S}_{ik} &= \sum^{l} \{N_s^l \mid i, k\} \\ &= \sum^{j} \hat{F}_{ijk} \end{aligned} \tag{14}$$

We define the *source strength* of site i, S_{ik}, as the *fraction* of larvae settling anywhere, given that each larva originated from source cell or group i at time k:

$$S_{ik} = \frac{\underline{S}_{ik}}{\rho A_i} \tag{15}$$

[1] Since we have over 8,000 coral reef cells and over 10,000 release days in our simulation, the full F matrices at cell-level would contain around 660×10^9 entries. Computing and storing these full F matrices at cell-level would therefore either require the use of sparse matrix objects, or chunked file writing. At present, the postprocessing scripts used in this study require around 600 core-hours on the JASMIN HPC for the entire 1993-2020 dataset. This is orders of magnitude less than the particle-tracking scripts, but it is still considerable. The use of sparse matrices or chunked file writing would add to the computational expense of postprocessing, and we have therefore not attempted it in this study. As a result, we only compute the F matrices at group level. We can, however, compute source strength at a cell level.

where ρA_i is the total number of larvae generated at source cell or group i at time k. This quantity is useful as it represents the likelihood of a larva generated at a source site settling anywhere. Note that A_i refers to the reef surface area of the *group* if i refers to a group.

Text S4: Data analysis

As described in the main text, to investigate physical drivers of source strength, we split reefs into 6 groups. We precisely define these groups as the following:

1. Reefs influenced by the East African Coastal Current, specifically all reefs in Tanzania, Kenya, and Somalia ($N = 1822$)
2. All reefs in Mozambique, excluding St. Lazarus Bank ($N = 995$)
3. All reefs in Madagascar ($N = 1695$)
4. Remote islands and reefs near the rapid Northeast Madagascar Current, specifically the Comoro islands, St. Lazarus Bank, Banc du Geyser, the Glorioso Islands, and the Aldabra and Farquhar Groups of Seychelles ($N = 980$)
5. Other remote islands, specifically the rest of Seychelles, remaining French scattered islands, Mauritius, and the Maldives ($N = 1036$)
6. The Chagos Archipelago ($N = 1560$)

The seven explanatory variables used to explain geographic variability in source strength were calculated as follows:

1. Mean surface current speed (m s^{-1}): the time-mean speed based on the daily mean velocity from 1993-2020, thereby averaging out sub-daily current variability.
2. Mean surface high-frequency current speed (m s^{-1}), based on the daily mean velocity from 1993-2020, with a high-pass filter to remove frequencies below $1/30$ d^{-1}.
3. Mean surface sub-daily current speed (m s^{-1}), based on the half-hourly mean velocity from 2016-2020, with a high-pass filter to remove frequencies below $1/30$ h^{-1}.
4. Nearby reef fraction (unitless), quantified as the reef fraction filtered by a 2D Gaussian kernel, with a standard deviation equal to the mean surface current speed at the cell multiplied by the minimum competency period t_c (roughly equal to the distance a larva may travel before its first chance of attaining competency).
5. Weighted connection distance (km), quantified as the average great-circle distance between a source cell and all of its downstream connections, weighted by the larval flux associated with each connection; in other words, the average great-circle distance a larva travels before settling.
6. Distance to land (km), quantified as the great-circle distance from the grid cell centre (ρ point) to the nearest coast (u/v point), identified by a Euclidean distance transform.

7. Mean source strength (unitless), quantified as the time-mean source strength for a cell from 1993-2019.

Supplementary Figures

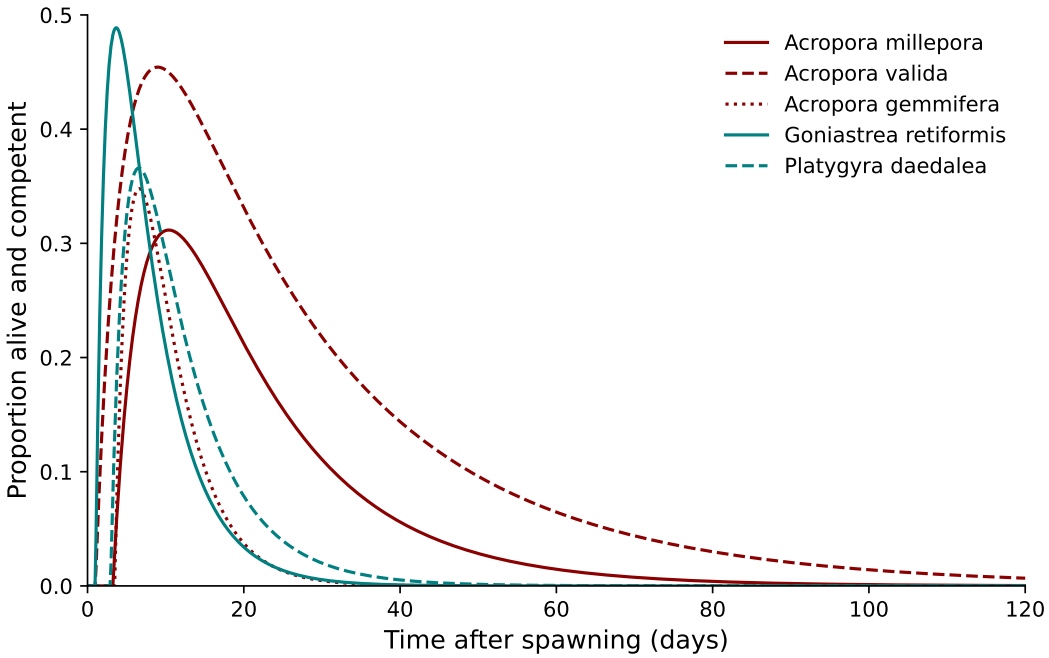

Supplementary Figure 1. Proportion of larvae alive and competent as a function of time, for *Goniastrea retiformis* (used in the main text) and four other coral species (see supplementary materials). Note that the minimum allowed competency period is set to 1 day in this study, contrary to the original form in Connolly and Baird (2010).

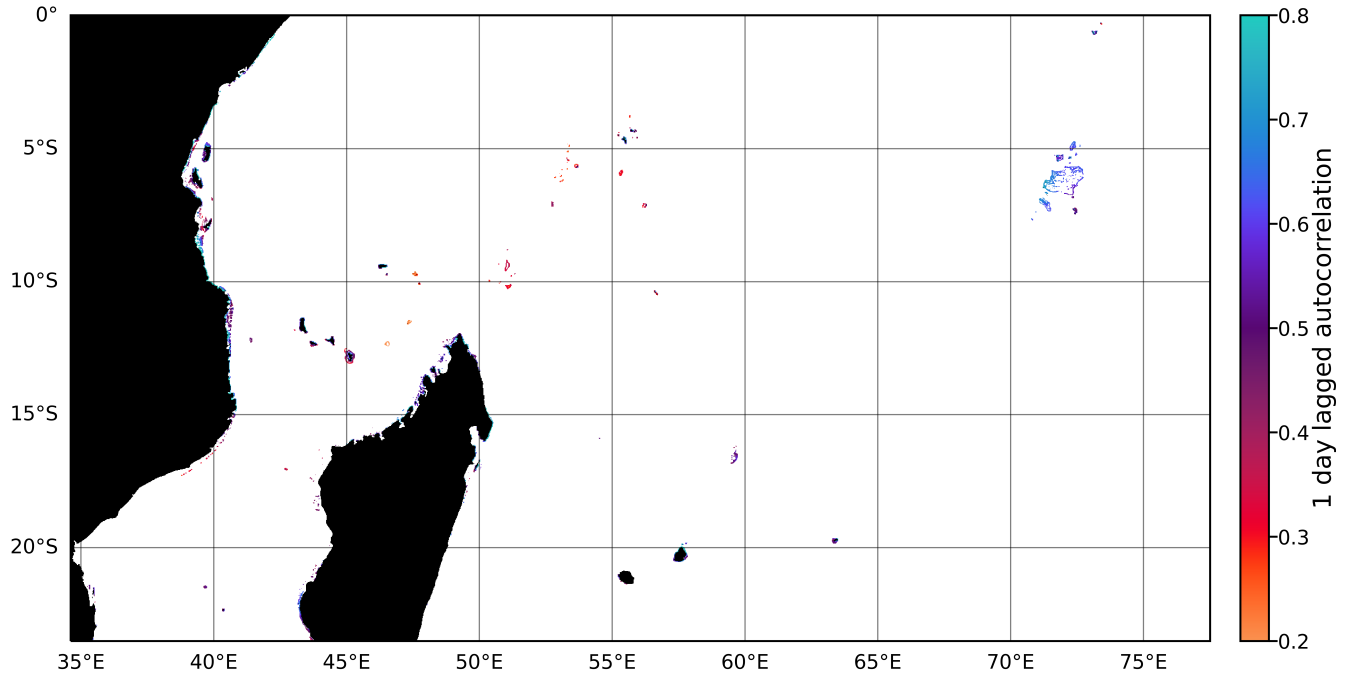

Supplementary Figure 2. Source strength autocorrelation as in Figure 2 in the main text, but for the full WINDS domain (see Supplementary Dataset 1 for the full high-resolution figure).

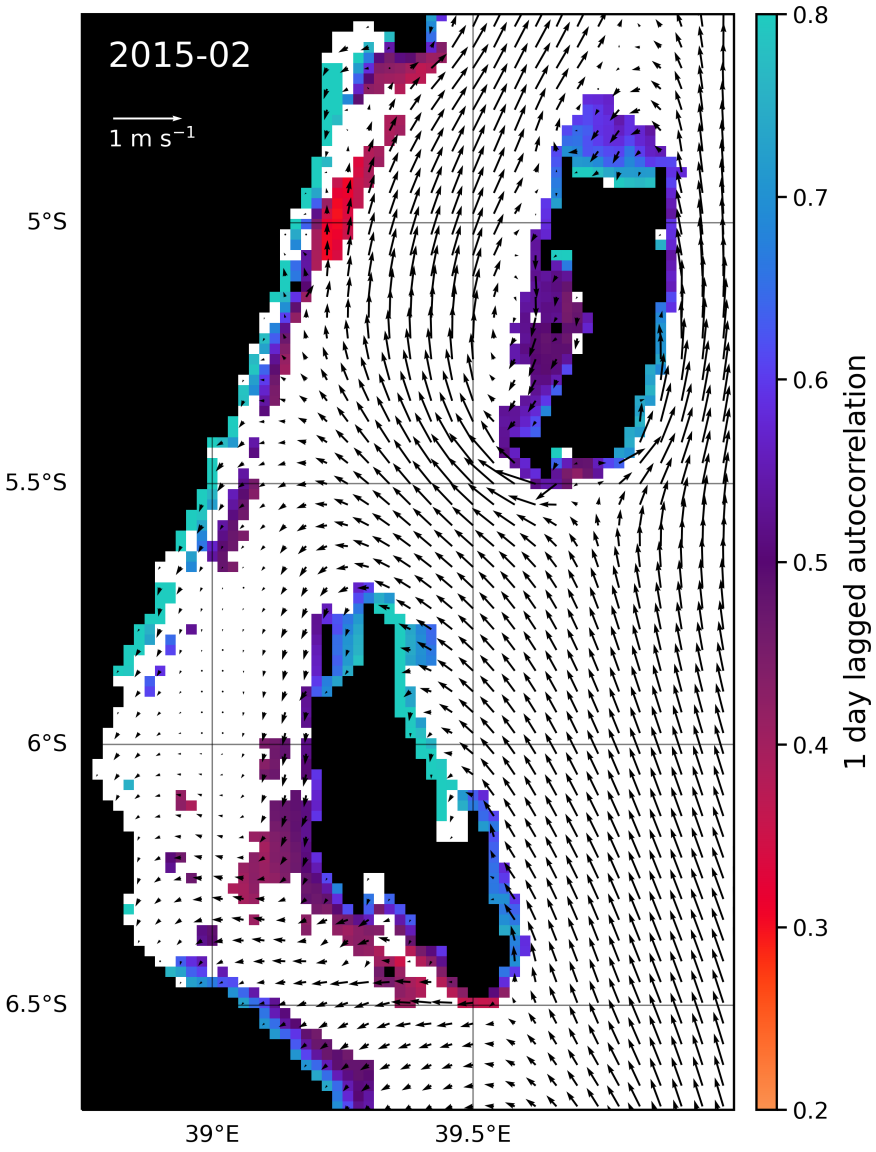

Supplementary Figure 3. Example of flow around Zanzibar and Pemba (February 2015), showing a number of flow reversals and deflections around capes and headlands, and correspondence with source strength autocorrelation.

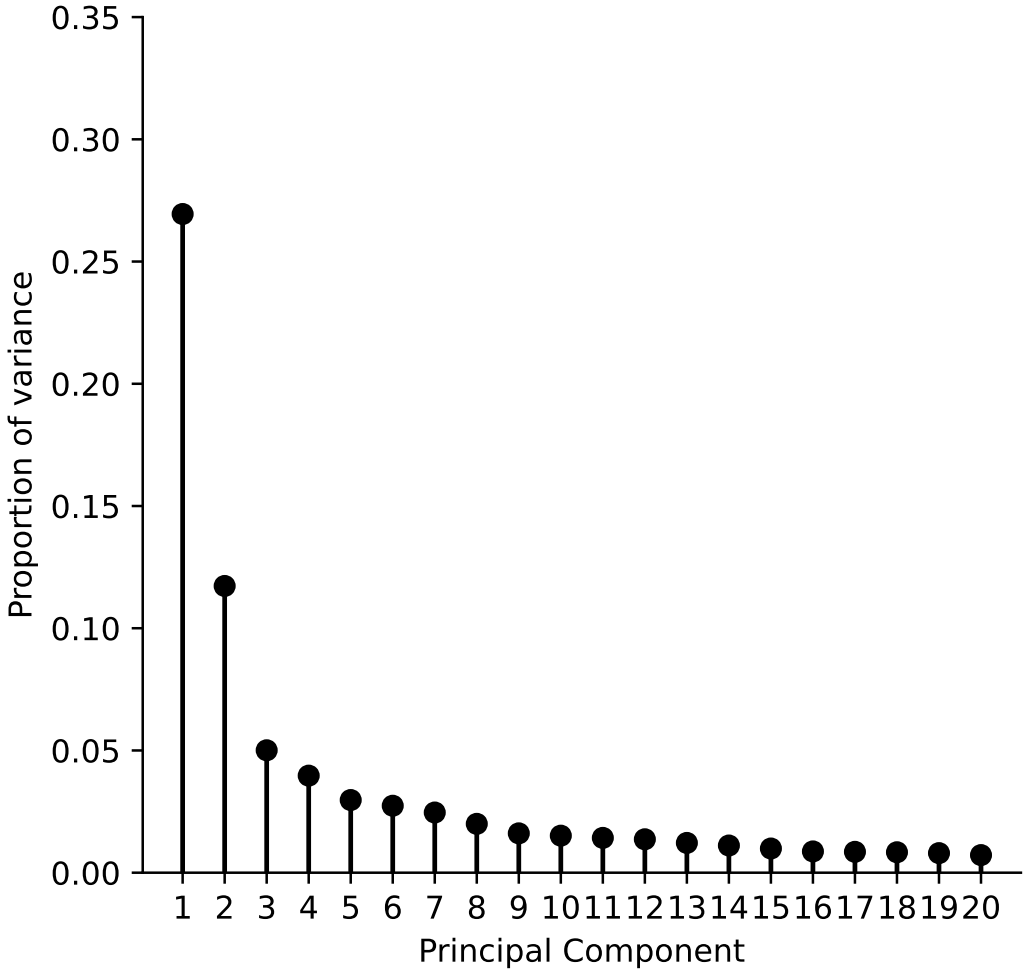

Supplementary Figure 4. Proportion of variance explained by the top principal components, from the EOF decomposition of the monthly-mean source strength matrix (see main text, section 3.2).

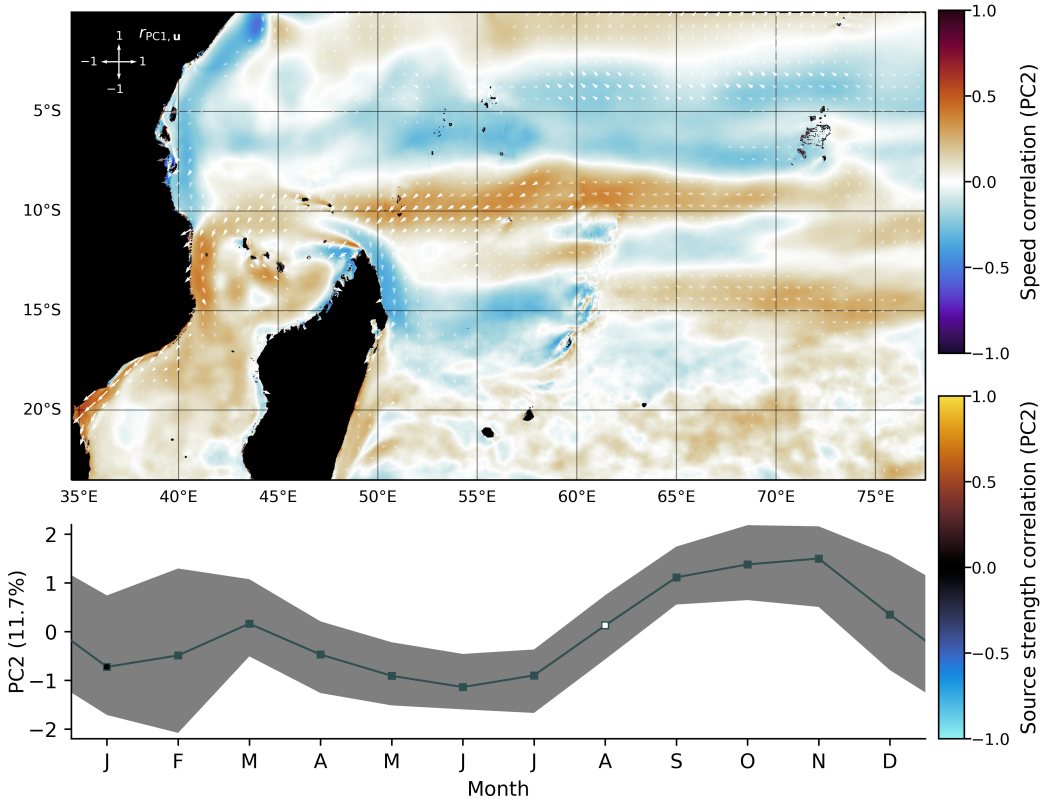

Supplementary Figure 5. As in Figure 5 in the main text, but for PC2.

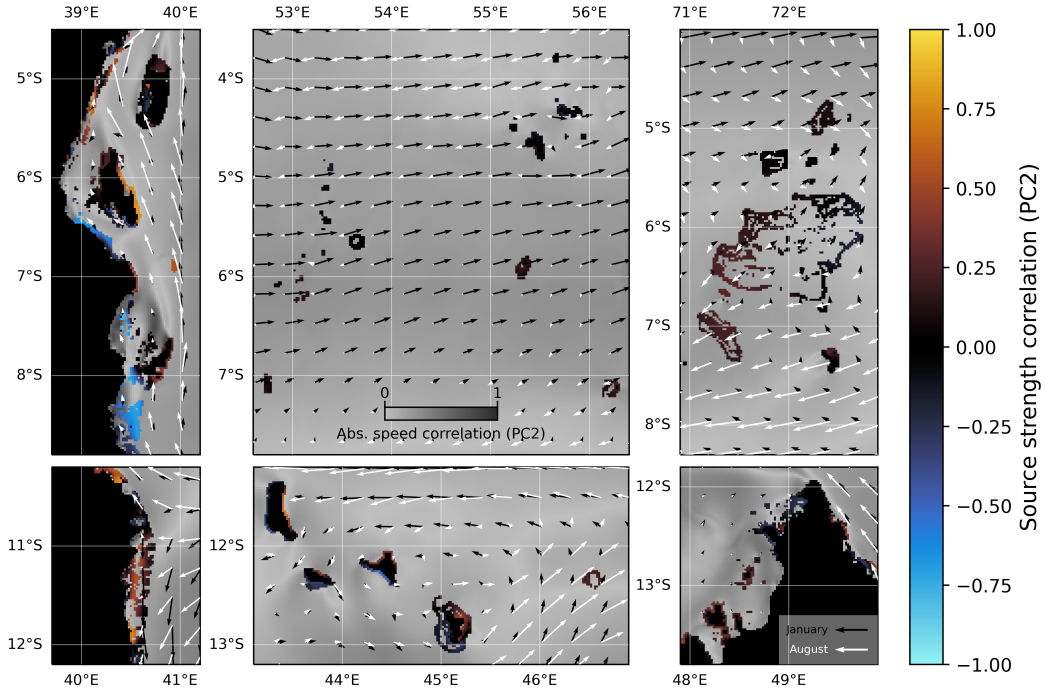

Supplementary Figure 6. As in Figure 6 in the main text, but for PC2.

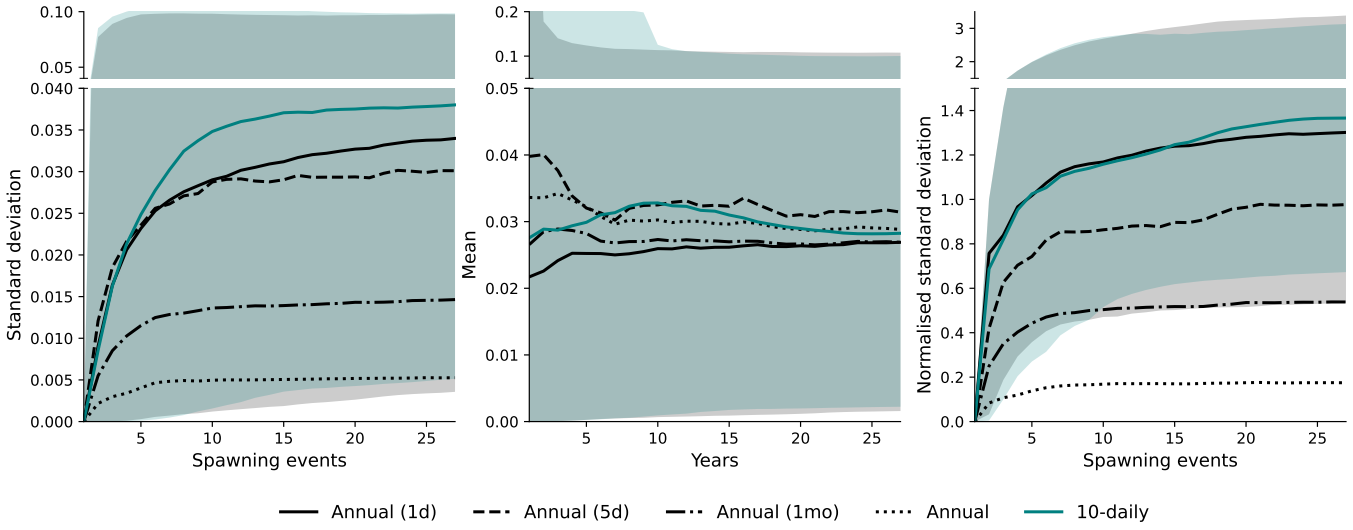

Supplementary Figure 7. Source strength standard deviation (left), mean (centre), and mean-normalised standard deviation (right) across reef cells as a function of the number of spawning events (as in Figure 7(a) in the main text)

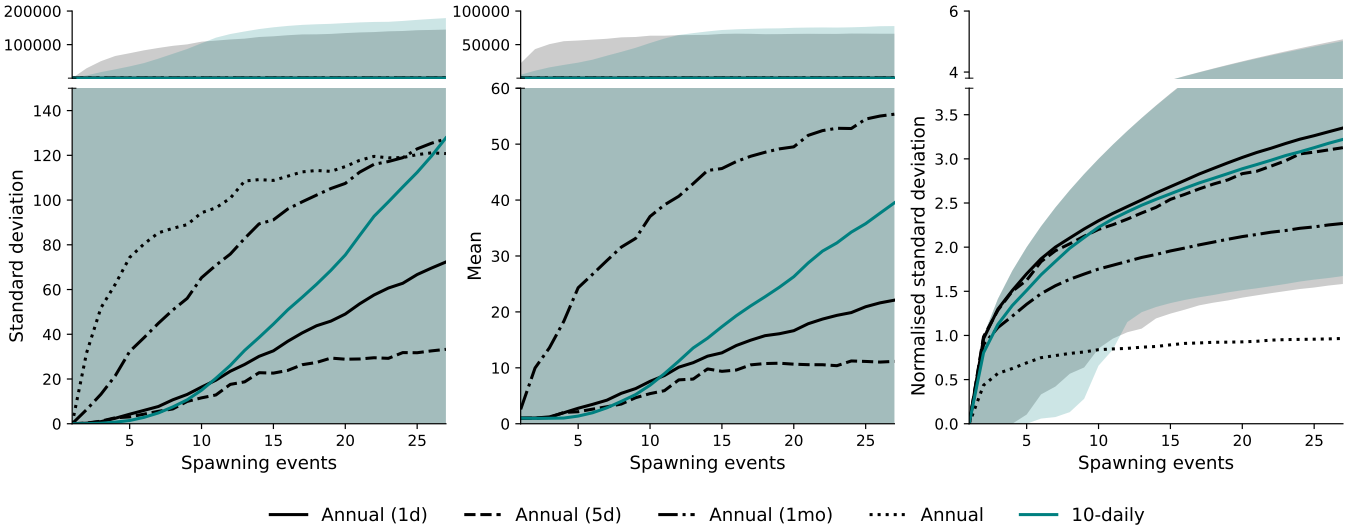

Supplementary Figure 8. Flux standard deviation (left), mean (centre), and mean-normalised standard deviation (right) across reef groups as a function of the number of spawning events (as in Figure 7(b) in the main text)

Supplementary Figure 9. (Backward) cumulated multistep implicit connectivity (CMIC) over 10 generations for 100 randomly chosen connections (which have nonzero connectivity for at least 1% of spawning events), i.e. similar to Figure 9 in the main text. Connections for each generation are selected based on a random time-slice during the northwest monsoon, and this is repeated 1000 times to obtain 1000 CMIC realisations. The teal bars show the 5^{th}-95^{th} percentiles across the 1000 realisations, and the white points represent the median. The black points represent the CMIC obtained from the time-mean potential connectivity matrix.

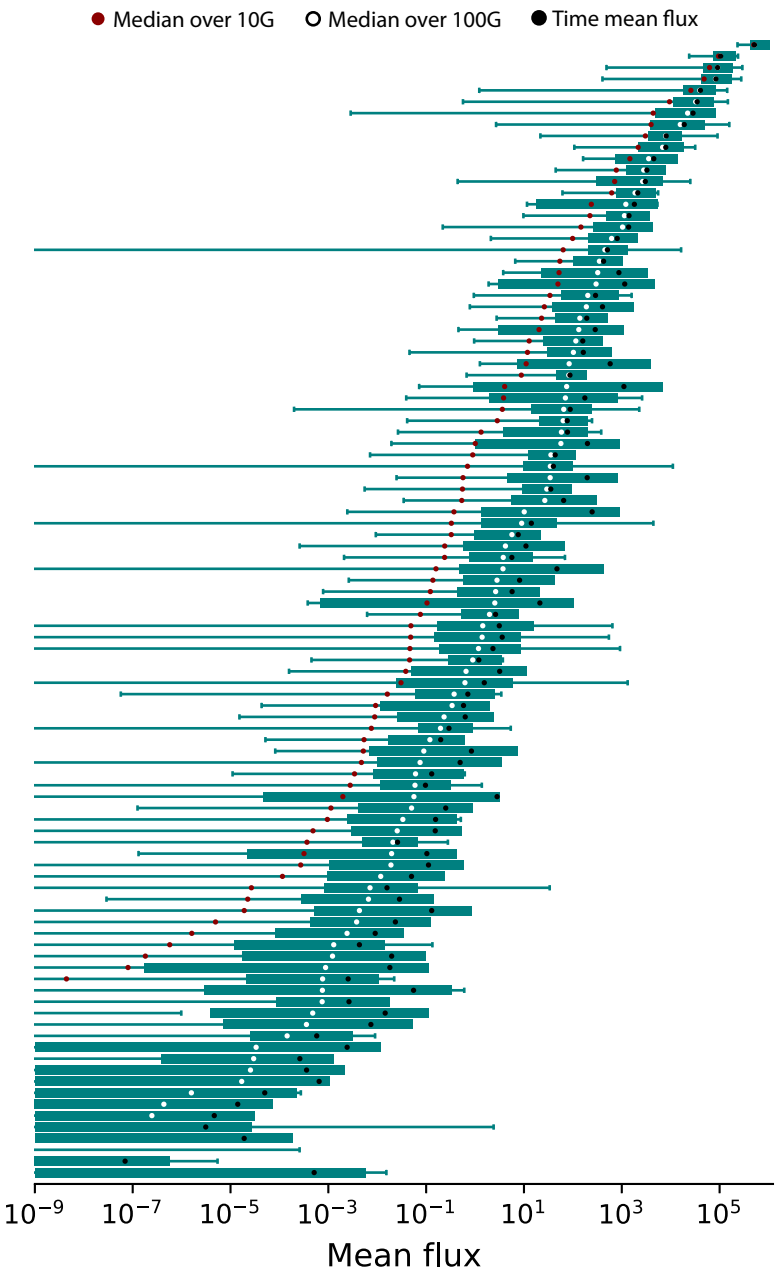

Supplementary Figure 10. Mean flux over 10 generations (median: red points) and 100 generations (median: white points) for 100 randomly chosen connections (which have nonzero connectivity for at least 1% of spawning events). Connections for each generation are selected based on a random time-slice during the northwest monsoon, and this is repeated 1000 times to obtain 1000 realisations. The teal bars show the 5^{th}-95^{th} percentiles across the 1000 realisations for 10 generations (thin bars) and 100 generations (thick bars). The black points represent the full time-mean flux. This is always greater than the median, due to the positive skew in flux.

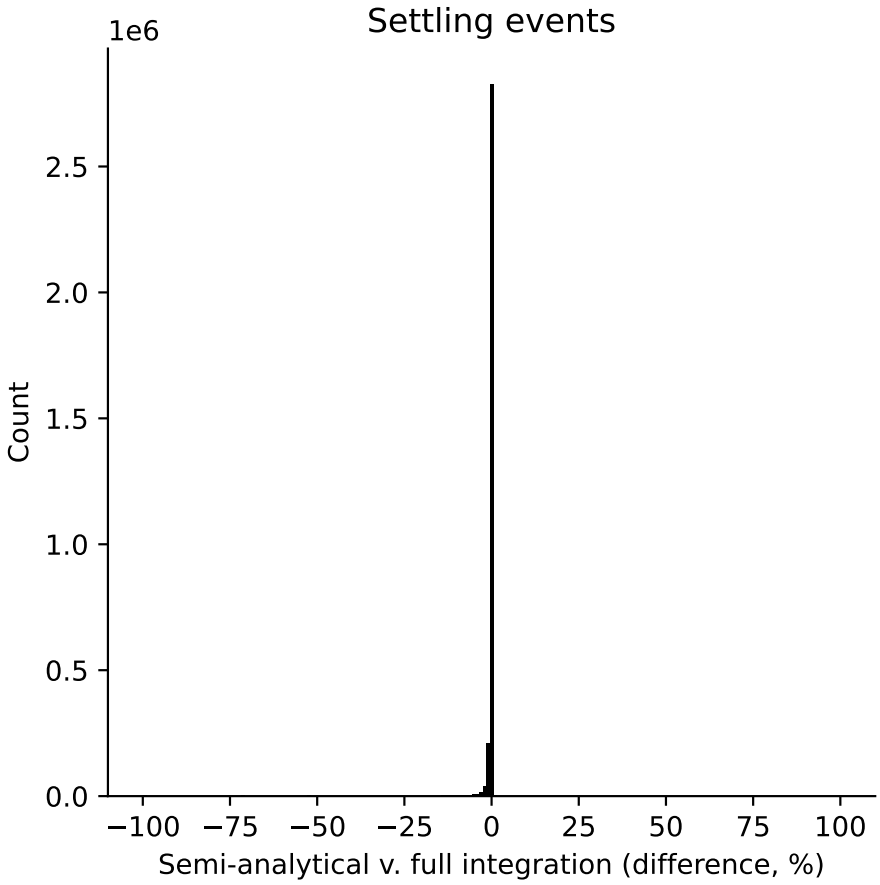

Supplementary Figure 11. Relative difference in percentage points for individual larval fluxes between the semi-analytical approach as described in Text S1 (with a single RK4 step per event), versus directly integrating equations 1 and 2 using RK4 at the SECoW time-step (10 minutes). This is based on a subsample of every 64th particle from the first spawning event (due to the computational cost associated with explicitly integrating these equations) for *Platygyra daedalea*. Note that there are extremely rare errors greater than 100%, but these represent a negligible proportion of events and are not visible on this scale.

Supplementary Animations

Supplementary Animation 1

Outbound connections from the Tanga reef group (see Figure 2(c)) in 2019, as a function of the spawning day. Connections are represented by circles at the centre of destination reef groups, and are shaded and sized depending on the number of larvae settling at that reef group from a particular spawning event (e.g. the state on 1/1/2019 gives the distribution of larval destinations from the spawning event on 1/1/2019, but the settling events took place over a range of days).

Supplementary Animation 2

Outbound connections from the Mahé NE reef group (see Figure 2(b)) in 2019, as a function of the spawning day.

Supplementary Animation 3

Outbound connections from the Rémire reef group (see Figure 2(c)) in 2019, as a function of the spawning day.

Supplementary Animation 4

Outbound connections from the Bassas da India reef group in 2019, as a function of the spawning day.

Supplementary Animation 5

Larval plume from spawning events in January 2019 (northwest monsoon) in NW Madagascar. Cells are shaded by the density of competent larvae (following *Acropora millepora* parameters, see Supplementary Table 1). Note the limited cross-shore transport and strong larval retention.

Supplementary Animation 6

Larval plume from spawning events in July 2019 (northwest monsoon) in NW Madagascar. Cells are shaded by the density of competent larvae (following *Acropora millepora* parameters, see Supplementary Table 1). Note the considerable cross-shore transport and weak larval retention.

Supplementary Tables

Species	Code	α^* (d^{-1})	β (d^{-1})	t_c (d)	λ (d^{-1})	ν	σ	μ_s (d^{-1})
A millepora	AM	0.18	0.050	3.239	0.043	0.57	0.0	1.0*
A valida	AV	0.22	0.031	1.0*	0.019	0.46	0.0	1.0*
A gemmifera	AG	0.39	0.145	3.471	0.067	1.0	0.0	1.0*
G retiformis	GR	0.58	0.096	1.0*	0.087	1.0	0.0	1.0*
P daedalea	PD	0.39	0.099	2.937	0.060	0.72	0.0	1.0*
P daedalea (fast)	PDf	0.39	0.099	2.937	0.060	0.72	0.0	2.0*
P daedalea (slow)	PDs	0.39	0.099	2.937	0.060	0.72	0.0	0.5*

Table 1. Biological parameters used for larval competency, mortality and settling in this study (see Section and Connolly and Baird (2010)). An asterisk indicates that the parameter used is not identical to Connolly and Baird (2010). For the minimum competency period t_c, this is due to the minimum of 1 day imposed by SECoW. For the settling rate μ_s, this is because settling rate was not included in the model of Connolly and Baird (2010).

Metric	AM	AV	AG	GR	PD	PDf	PDs
r_{1d} at Tanga	0.87	0.89	0.85	0.84	0.86	0.88	0.85
r_{1d} at Mah'e NE	0.60	0.64	0.60	0.65	0.61	0.62	0.60
r_{1d} at Rémire Island	0.24	0.26	0.24	0.27	0.24	0.28	0.22
99^{th} pct. autocorrelation τ (d)	13.7	14.8	9.2	8.2	9.9	9.9	10.0
Top r_{1d} predictor (EACC)	WCD	WCD	WCD	WCD	WCD	WCD	WCD
Top r_{1d} predictor (Mozambique)	WCD	WCD	Land dist.	Land dist.	Land dist.	Land dist.	WCD
Top r_{1d} predictor (Madagascar)	Land dist.	Land dist.	Land dist.	Land dist.	Land dist.	Land dist.	Land dist.
Top r_{1d} predictor (NEMC)	Speed	Speed	WCD	WCD	WCD	WCD	WCD
Top r_{1d} predictor (Other islands)	HF Speed	HF Speed	WCD	WCD	WCD	WCD	WCD
Top r_{1d} predictor (Chagos)	SD Speed	SD Speed	NRF	NRF	NRF	SD Speed	NRF
Monthly source strength explained by mean seasonal cycle (all)	26.6%	29.3%	24.8%	28.8%	25.6%	26.0%	25.2%
Monthly source strength explained by mean seasonal cycle (East Africa)	67.2%	70.5%	62.9%	64.2%	65.0%	64.8%	64.2%
Monthly source strength variance explained by PC1	29.3%	31.1%	25.8%	30.9%	26.9%	26.2%	27.3%
Monthly source strength variance explained by PC2	12.1%	11.7%	11.8%	10.9%	11.7%	11.3%	12.1%
% of spawning events accounting for half of settling larvae (median)	13.6%	17.7%	12.2%	17.4%	13.3%	14.4%	12.5%
% of spawning events accounting for half of settling larvae (upper decile)	4.4%	6.7%	3.4%	5.1%	4.0%	4.4%	3.6%
Reefs with $\leq$1% of spawning events accounting for half of settling larvae	26	10	113	10	47	26	76
Annual source strength corr. with individual months (R^2)	0.55-0.88	0.57-0.89	0.58-0.88	0.59-0.90	0.58-0.89	0.59-0.89	0.57-0.88
NW monsoon source strength corr. with individual months (R^2)	0.69-0.92	0.71-0.93	0.76-0.94	0.78-0.95	0.75-0.94	0.75-0.94	0.75-0.94

Table 2. Comparison of several example metrics from the main text across the seven sets of biological parameters described in Table 1. Entries for 1-day lagged source strength autocorrelation predictors are as follows: WCD (weighted connection distance), Land dist. (distance to land), Speed (mean speed), HF Speed (mean speed in $1/30$-1 d^{-1} frequency range), SD Speed (mean speed in $< 1/30$ h^{-1} frequency range), NRF (nearby reef fraction).

References

Connolly, S. R. and Baird, A. H.: Estimating dispersal potential for marine larvae: Dynamic models applied to scleractinian corals, Ecology, 91, 3572–3583, https://doi.org/10.1890/10-0143.1, 2010.

Figueiredo, J., Thomas, C. J., Deleersnijder, E., Lambrechts, J., Baird, A. H., Connolly, S. R., and Hanert, E.: Global warming decreases connectivity among coral populations, Nature Climate Change, 12, 83–87, https://doi.org/10.1038/s41558-021-01248-7, publisher: Springer US, 2022.

Harii, S. and Kayanne, H.: Larval dispersal, recruitment, and adult distribution of the brooding stony octocoral Heliopora coerulea on Ishigaki Island, southwest Japan, Coral Reefs, 22, 188–196, https://doi.org/10.1007/s00338-003-0302-9, 2003.

Hartmann, A. C., Marhaver, K. L., and Vermeij, M. J.: Corals in Healthy Populations Produce More Larvae Per Unit Cover, Conservation Letters, 11, 1–12, https://doi.org/10.1111/conl.12410, 2018.

Hata, T., Madin, J. S., Cumbo, V. R., Denny, M., Figueiredo, J., Harii, S., Thomas, C. J., and Baird, A. H.: Coral larvae are poor swimmers and require fine-scale reef structure to settle, Scientific Reports, 7, 1–9, https://doi.org/10.1038/s41598-017-02402-y, publisher: Springer US, 2017.

Holstein, D. M., Paris, C. B., Vaz, A. C., and Smith, T. B.: Modeling vertical coral connectivity and mesophotic refugia, Coral Reefs, 35, 23–37, https://doi.org/10.1007/s00338-015-1339-2, publisher: Springer Berlin Heidelberg, 2016.

Kingsford, M. J., Leis, J. M., Shanks, A., Lindeman, K. C., Morgan, S. G., and Pineda, J.: Sensory environments, larval abilities, and local self-recruitment, BULLETIN OF MARINE SCIENCE, 70, 2002.

Li, J., Knapp, D. E., Fabina, N. S., Kennedy, E. V., Larsen, K., Lyons, M. B., Murray, N. J., Phinn, S. R., Roelfsema, C. M., and Asner, G. P.: A global coral reef probability map generated using convolutional neural networks, Coral Reefs, 39, 1805–1815, https://doi.org/10.1007/s00338-020-02005-6, publisher: Springer Berlin Heidelberg, 2020.

Mitarai, S., Siegel, D. A., Watson, J. R., Dong, C., and McWilliams, J. C.: Quantifying connectivity in the coastal ocean with application to the Southern California Bight, Journal of Geophysical Research: Oceans, 114, 1–21, https://doi.org/10.1029/2008JC005166, 2009.

Mulla, A. J., Takahashi, C.-h. L. S., and Nozawa, Y.: Photo-movement of coral larvae influences vertical positioning in the ocean, Coral Reefs, https://doi.org/10.1007/s00338-021-02141-7, publisher: Springer Berlin Heidelberg, 2021.

Okubo, A.: Oceanic diffusion diagrams, Deep-Sea Research and Oceanographic Abstracts, 18, 789–802, https://doi.org/10.1016/0011-7471(71)90046-5, 1971.

Reijnders, D., Deleersnijder, E., and van Sebille, E.: Simulating Lagrangian Subgrid-Scale Dispersion on Neutral Surfaces in the Ocean, Journal of Advances in Modeling Earth Systems, 14, https://doi.org/10.1029/2021MS002850, 2022.

Szmant, A. M. and Meadows, M. G.: Developmental changes in coral larval buoyancy and vertical swimming behavior: Implications for dispersal and connectivity, Proceedings of the 10th International Coral Reef Symposium, 1, 431–437, 2006.

Tay, Y. C., Guest, J. R., Chou, L. M., and Todd, P. A.: Vertical distribution and settlement competencies in broadcast spawning coral larvae: Implications for dispersal models, Journal of Experimental Marine Biology and Ecology, 409, 324–330, https://doi.org/10.1016/j.jembe.2011.09.013, publisher: Elsevier B.V., 2011.

Thompson, D. M., Kleypas, J., Castruccio, F., Curchitser, E. N., Pinsky, M. L., Jönsson, B., and Watson, J. R.: Variability in oceanographic barriers to coral larval dispersal: Do currents shape biodiversity?, Progress in Oceanography, 165, 110–122, https://doi.org/10.1016/j.pocean.2018.05.007, publisher: Elsevier, 2018.

Uchiyama, Y., Odani, S., Kashima, M., Kamidaira, Y., and Mitarai, S.: Influences of the Kuroshio on Interisland Remote Connectivity of Corals Across the Nansei Archipelago in the East China Sea, Journal of Geophysical Research: Oceans, 123, 9245–9265, https://doi.org/10.1029/2018JC014017, 2018.

van Sebille, E., Griffies, S. M., Abernathey, R., Adams, T. P., Berloff, P., Biastoch, A., Blanke, B., Chassignet, E. P., Cheng, Y., Cotter, C. J., Deleersnijder, E., Döös, K., Drake, H. F., Drijfhout, S., Gary, S. F., Heemink, A. W., Kjellsson, J., Koszalka, I. M., Lange, M., Lique, C., MacGilchrist, G. A., Marsh, R., Mayorga Adame, C. G., McAdam, R., Nencioli, F., Paris, C. B., Piggott, M. D., Polton, J. A., Rühs, S., Shah, S. H., Thomas, M. D., Wang, J., Wolfram, P. J., Zanna, L., and Zika, J. D.: Lagrangian ocean analysis: Fundamentals and practices, Ocean Modelling, 121, 49–75, https://doi.org/10.1016/j.ocemod.2017.11.008, 2018.